Cooperative low-rank models for removing stripe noise from OCTA images

Xiyin Wu, Dongxu Gao, Davide Borroni, Savita Madhusudhan, Zhong Jin, Yalin Zheng

***Abstract*—Optical coherence tomography angiography (OCTA) is an emerging non-invasive imaging technique for imaging the microvasculature of the eye based on phase variance or amplitude decorrelation derived from repeated OCT images of the same tissue area. Stripe noise occurs during the OCTA acquisition process due to the involuntary movement of the eye. To remove the stripe noise (or 'destriping') effectively, we propose two novel image decomposition models to simultaneously destripe all the OCTA images of the same eye cooperatively: cooperative uniformity destriping (CUD) model and cooperative similarity destriping (CSD) model. Both the models consider stripe noise by low-rank constraint but in different ways: the CUD model assumes that stripe noise is identical across all the layers while the CSD model assumes that the stripe noise at different layers are different and have to be considered in the model. Compared to the CUD model, CSD is a more general solution for real OCTA images. An efficient solution (CSD+) is developed for model CSD to reduce the computational complexity. The models were extensively evaluated against state-of-the-art methods on both synthesized and real OCTA datasets. The experiments demonstrated not only the effectiveness of the CSD and CSD+ models in terms of peak signal-to-noise ratio (PSNR) and structural similarity index (SSIM) and CSD+ is twice faster than CSD, but also their beneficiary effect on the vessel segmentation of OCTA images. We expect our models will become a powerful tool for clinical applications.**

***Index Terms*—OCTA destriping, cooperative, retina vessel segmentation, low-rank, total variation.**

I. Introduction

Optical coherence tomography angiography (OCTA) is a new promising non-invasive imaging technique for imaging blood vessels up to capillary levels [1], which previously can only be achieved by invasive and potentially life-threatening angiographic techniques [2]. OCTA has shown great potentials in the management of a wide range of retinal diseases such as diabetic retinopathy and age-related macular degeneration [1]. With the advances of the OCTA techniques, there are still challenges in terms of acquisition quality and quantitative analysis to fulfill its full clinical potential. In this paper, we propose new cooperative solutions to remove stripe noise ('destripe') which is an inherent nature of OCTA images during its acquisition process.

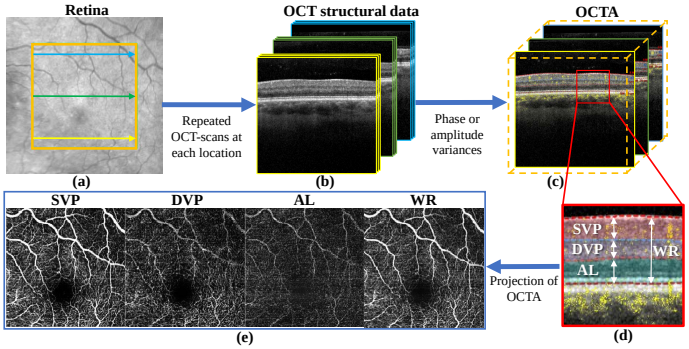

Fig. 1. Acquisition process of OCTA image. (a) Infrared image illustrating the scanning position of OCT. (b) OCT structural volume with repeated scans at each scanning location. (c) OCTA volume data (yellow dots) superimposed on the OCT image. OCTA are acquired by phase or amplitude variances from repeated OCT scans at each location. (d) A zoomed in region of (c). (e) Projection of OCTA map by selecting certain layers: SVP, DVP, AL and WR.

OCTA is a functional extension of well-established optical coherence tomography (OCT) imaging to visualize the micro-vasculature of the eye [3]. Fig.1 illustrates the acquisition process of OCTA images. OCTA reconstructs blood vessels by detecting moving particles such as red blood cells in the tissue by deriving phase [4] or amplitude [5] variances from the repeated OCT scans at the same location. A 3D OCTA map can be produced by taking sequential cross-sectional OCTA scans of the scanned tissue [6]. For the ease of visualizing the retinal vessels, projections of the acquired 3D OCTA map into 2D en face images are often used. As shown in Fig. 1(d) and (e), retinal vessels at a certain depth of the retina can be generated by selecting certain layers of the retina from the projection. For example, the vessels of the whole retina (WR) are set from the internal limiting membrane (ILM) to the Bruch's membrane, superficial vascular plexus (SVP) is from the ILM to the outer boundary of the inner plexiform layer (IPL), deep vascular plexus (DVP) is from the outer boundary of the IPL to the external boundary of the outer plexiform layer (OPL) and avascular layer (AL) is from the outer boundary of the OPL to the Bruch's membrane [7].

It usually takes several seconds (depending on the OCT devices, e.g. 3-5 seconds [8]) to acquire a 3D OCTA map, thus OCTA images are inevitably susceptible to motion artifacts caused by the involuntary eye movements [8]. Large and rapid eye motions like microsaccade will cause a momentary change in location of the scan, and will produce visible horizontal or vertical white stripes in the OCTA images [9]. During the

Manuscript received December 31, 2019. *(Corresponding author: Zhong Jin, Yalin Zheng.)*

X. Wu is with the Key Laboratory of Intelligent Perception and System for High-Dimensional Information of Ministry of Education, School of Computer Science and Engineering, Nanjing University of Science and Technology, Nanjing 210094, China, and also with the Department of Eye and Vision Science, Institute of Ageing and Chronic Disease, University of Liverpool, Liverpool L7 8TX, UK. D Gao and Y Zheng are with the Department of Eye and Vision Science, University of Liverpool, Liverpool, L7 8TX, UK. D Borroni and S Madhusudhan are with St. Paul's Eye Unit, Royal Liverpool University Hospital, Liverpool L7 8XP

Xiyin Wu is supported by the National Natural Science Foundation of China under Grant Nos 61872188, U1713208, 61972204, 61672287, 61861136011, 61773215. Dongxu Gao is supported by EPSRC under grant EP/R014094/1.

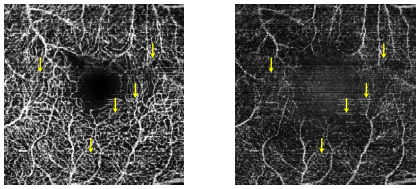

Fig. 2. Illustration of residual stripe noise in two different OCTA layers. Left: Deep vascular plexus (DVP).Right: Avascular layer (AL). Both of two OCTA images are corrupted by similar stripe noise (yellow arrows).

eye movements, the adjacent OCT-scans cannot match because they are from different tissues of the eye and give rise to large decorrelation. These stripe artifacts will unfortunately affect the visualization, interpretation and analysis of OCTA images and even the clinical diagnosis [10].

Stripe noise could be reduced if the acquisition time could be shortened by increasing the scanning speed. However, it is not always an easy solution due to the limitation of hardware configurations and cost implications. As a compromise, commercial devices have adopted different proprietary motion detection and correction strategies to alleviate the problem. For instance, scanning laser ophthalmoscope (SLO) has been used to resume the scan by adjusting the scan to the right location [10], [11]. Orthogonal registration combined the information in horizontal and vertical OCT volume scans to produce one OCTA map [12]. Although these motion correction methods can alleviate the problem, stripe noise in the form of residual non-homogeneous lines and distorted lines remain (see Fig. 2). Moreover, these strategies cause prolonged scanning time due to the tracking and reposition need and will fail when patients have poor fixations or their eyes keep moving. Some other strategies were proposed for OCTA stripes removal. Zang et al. [8] presented a parallel-stripe registration solution to correct large transverse motion artifacts on an ultra high-speed OCTA system. However, less dense vessel density was generated because only the information from one scan was used. To eliminate the bright short lines in OCTA images, Yang et al. [13] compared three domain based destriping methods and proved that the nonsubsampled contourlet domain [14] performs best. Its effectiveness was only proved for short lines elimination without bright long stripes. Although there has been some success in OCTA image destriping, further effort is needed to solve this challenging problem.

Stripe noise exists in other imaging modalities and a plethora of destriping methods are in the literature. These techniques are classified into four categories: image filtering, statistical matching, deep learning and optimization modeling. Stripe noise is high-frequency in nature, many *image filtering methods* design low pass filters to reduce stripe noise in the frequency domain. Munch et al. [15] combined wavelet and Fourier analysis to remove the stripe artifacts in electron microscopy and X-ray phase contrast images. Shu et al. [16] designed a divide-and-conquer strategy to split the Fourier spectrum for destriping atomic force microscopy (AFM) biomolecular images. Liang et al. [14] used the nonsubsampled contourlet transform to remove multidirectional stripe in Light-sheet fluorescence microscopy (LSFM). Although image filtering based methods are relatively easy to implement and process images efficiently, they generally perform well for periodic stripe noise and do not utilize the properties of the underlying image. *Statistical matching methods* calculate the statistical properties (e.g. histogram or moment) of an image as the reference and then adjust the intensity distribution of each image to the reference distribution [17], [18]. Although these methods are computationally efficient, their performance becomes unstable when the image background is complex or the stripe noise is irregular [18]. *Deep learning methods* have recently attracted increasing attention for image analysis. An HSI-DeNet was proposed for the restoration of hyperspectral images [19] and a deep multiscale residual network (DMRN) was proposed for infrared nonuniform correction [20], both of which have shown promising results in destriping. In a more recent work [21], Chang et al. reviewed existing destriping methods in remote sensing imaging systems and proposed a two-stream convolutional neural network (CNN) destriping model to simultaneously model the stripe and image. Wavelet was incorporated into this CNN model for better directional feature representation. This model has shown superior performance to previous methods. Along the same line, a two-stage deep CNN model was proposed for denoising medical images where two CNN sub-networks were used for simultaneous noise prediction and image reconstruction [22]. These works highlight the potential of deep learning in destriping as well as their limitations. For instance, it takes a long time to train these deep learning models and the training often requires a large number of images as well as ground truth images (e.g. clean images for destriping). It is often hard to obtain ground truth images in real applications. *Optimization modeling methods* have recently become the mainstay for image destriping [23], [24], [25]. Considering an image consisted of a noisy image and a clean image, these models retrieve the clean image by modeling some assumptions and priors of clean image or stripe noise. In [26], an anisotropic total variation regularization method was used to preserve the edges and details of remote sensing images. This method treated the stripes as the large edges by the isotropic total variation model and did not model the stripe characteristic individually. Supposing all spectra in the spectral difference space were in the same low-rank subspace, Sun et al. [24] utilized the low-rank representation to remove stripe noise in hyperspectral images. Chang et al. [25] treated the destriping task as an image decomposition problem by considering the stripe and clean images equally and decoupled completely. As singular-value decomposition during stripe component optimization is time-consuming for big matrix, this method is not efficient for large size images. Overall, optimization based models are very promising owing to its mathematical rigor, flexibility and performance. On the other hand, they are relatively slow because the models are solved by iterative solvers.

Inspired by the optimization based models, we propose two novel cooperative optimization models for OCTA destriping. To make our model effective and efficient, four factors specific to OCTA destriping problems have been considered. First, the priors used in other imaging modalities are not fit for purpose and the priors suitable for OCTA have to be sought. Second, our models should be flexible and effective for both vertical and horizontal directions as the OCTA scan pattern changes.

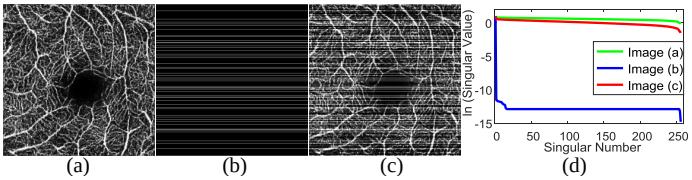

Fig. 3. Low-rank prior of stripes. (a) Simulated clean OCTA image. (b) Horizontal stripe noise. (c) Image (a) degraded by horizontal stripe noise (b). (d) Natural logarithm of singular values of (a), (b) and (c).

Third, OCTA images generated from different layers reveal similar stripe noise patterns, as shown in Fig. 2. This is unique to other imaging modalities whilst it can be exploited to build more effective destriping models. Finally, the efficiency of the models should be acceptable for clinic usage.

Our proposed models have made a step forward in terms of performance and sped with the contributions as follows. First, the proposed two models are novel for OCTA destriping in which low-rank prior is chosen for the stripe component whereas the clean image is leveraged by anisotropic total variation prior. Second, the proposed destriping models explicitly consider the relationships of stripe noises across the OCTA images from different layers. Third, an efficient accelerated solution has been proposed whereas a robust orthonormal subspace learning approach is introduced to speed up the low lank sub-problem while a homotopy method is used to accelerate the total variation sub-problem. Fourth, the proposed models have been validated not only on their destriping effectiveness on two synthetic datasets and one real OCTA dataset, but also on their influences on OCTA vessel segmentation. The results showed that the performance of vessel segmentation can be improved after applying our methods.

The paper is organized as follows. Section II presents the proposed models. Section III describes the datasets and performance metrics. Section IV investigates the destriping results and explores their influence on the vessel segmentation. A short discussion and conclusion are given in Section V.

II. Method

In this section, we describe in detail the proposed two OCTA image destriping models. First, the stripe degradation process and the problem formulation in destriping are given whereas the rationale for choosing low-rank prior and conventional anisotropic total variation prior is discussed. The cooperative uniformity destriping (CUD) model assuming identical stripe noise across all the images is then presented followed by the description of the cooperative similarity model (CSD) considering stripe noise is only similar among different layers. Finally, an acceleration solution CSD+ for CSD is presented.

A. Problem Formulation

OCTA image destriping is formulated as an image decomposition problem. Let $I_i, C_i, S_i, N_i \in \mathbb{R}^{m\times n}$ be the ith layer of an acquired OCTA map, corresponding desired clean image, additive stripe component and small noise respectively. m, n represent the number of rows and columns and $i = 1, \cdots, q$, q is the total layer number of OCTA images (e.g. here we considered 4 layers: SVP, DVP, AV and WR). The image degradation process is formulated as $I_i = C_i + S_i + N_i$. The problem to simultaneously estimate both C_i and S_i can be formulated below:

$$\min_{C_i,S_i} \sum_{i=1}^{q} (\frac{1}{2}\|C_i + S_i - I_i\|_F^2 + \tau R(C_i) + \lambda R(S_i)) \quad (1)$$

where $\|.\|_F$ is the Frobenius norm. The first fidelity term in Eq. (1) enforces that the clean image C_i and additive stripe noise S_i will not deviate too much from the degraded image I_i. $R(C_i)$ and $R(S_i)$ are constraints for the clean image and stripe noise, respectively. τ and λ are two positive parameters balancing the three terms. The model (1) estimates q clean images simultaneously when $q > 1$, while only evaluates clean image one by one when $q = 1$ and is equivalent to the model [25] in this special case.

B. Priors of Stripe Noise and Clean OCTA Image

The stripe noise in OCTA images has a salient direction feature in either horizontal or vertical direction. To analyze the characteristic of stripe noise, we constructed an image with horizontal stripes as shown in Fig. 3(b). It is found that the rank of this matrix is equal to 1 and so that the rank of vertical stripe matrix is also equal to 1. The rank value of stripe matrix indicates that its spanned subspace can be expressed as low-rank constraint, which is expressed as:

$$R(S_i) = \text{rank}(S_i) \quad (2)$$

Moreover, we studied the rank change before and after the OCTA image degraded by stripe noise. A synthesized 256x256 clean OCTA image (see Fig. 3(a)) is corrupted by adding the horizontal stripes in Fig. 3(b) and the resulting degraded image is shown in Fig. 3(c). Their corresponding natural logarithm of singular values are depicted in Fig. 3(d). While the singular values of both the clean OCTA image and degraded image approximate to zero ($ln(0) = -\infty$) at rank 256 slowly, the singular value of the stripe image approximate to zero at rank 1 rapidly. The trends of clean and degraded OCTA images in Fig. 3(d) are similar and their ranks are both equal to 256. We can conclude that the rank of OCTA image is higher than the rank of stripes, and the low-rank constraint of stripe noise will not affect the image content.

Total variation (TV) is a widely used regularizer for reducing noise while preserving edges in images [27]. For OCTA images, anisotropic TV regularization can obtain sharper boundaries in the clean image, which is important for subsequent processing, such as vessel segmentation. As the stripe noise exists in horizontal or vertical direction, the anisotropic TV regularization can adapt these two situations by loosening constraints on the stripe noise direction. The formulation of anisotropic TV regularization is given as:

$$R(C_i) = \|C_i\|_{\text{TV}} = \|\nabla_x C_i\|_1 + \|\nabla_y C_i\|_1 \quad (3)$$

where $\|\cdot\|_1$ is L_1 norm indicating the sum of absolute value of the matrix elements. ∇_x, ∇_y are the row and column derivative operators respectively.

C. Cooperative Uniformity Destriping (CUD)

If the stripe noise across all the images I_i from the same volume are identical (i.e. all of $S_i(i = 1, \cdots, q)$ are same in Eq. (1)), destriping all the OCTA images can become more efficient by a cooperative uniformity destriping (CUD) model than processing them separately as follows.

$$\min_{C_i,S} \sum_{i=1}^{q} \frac{1}{2}\|C_i + S - I_i\|_F^2 + \tau \sum_{i=1}^{q} \|C_i\|_{\mathrm{TV}} + \lambda \mathrm{rank}(S) \quad (4)$$

where S is introduced to represent the common stripe noise in all layers ($S = S_1, \cdots, S_q$). Since the rank constraint is non-convexity, nuclear norm is used to substitute the low-rank constraint [28]. This substitution is a common trick and has proved formally equivalent under suitable conditions [29]. The nuclear norm based CUD model is given by

$$\min_{C_i,S} \sum_{i=1}^{q} \frac{1}{2}\|C_i + S - I_i\|_F^2 + \tau \sum_{i=1}^{q} \|C_i\|_{\mathrm{TV}} + \lambda \|S\|_* \quad (5)$$

where $\|S\|_*$ is the nuclear norm of S.

Model (5) can be solved by the alternative direction multiplier method (ADMM) [30], which optimizes C_i and S alternatively. It converts the problem (5) to two sub-problems: a nuclear norm regularized and a L_1 regularized based minimization problem:

$$\hat{S} = \arg\min_{S} \sum_{i=1}^{q} \frac{1}{2}\|C_i + S - I_i\|_F^2 + \lambda \|S\|_* \quad (6)$$

$$\hat{C}_i = \arg\min_{C_i} \sum_{i=1}^{q} (\frac{1}{2}\|C_i + S - I_i\|_F^2 + \tau_x \|\nabla_x C_i\|_1 + \tau_y \|\nabla_y C_i\|_1) \quad (7)$$

where $\|\cdot\|_1$ represents the sum of absolute value of matrix elements. The weights τ_x and τ_y are set to $5e^{-3}$ and $5e^{-4}$ in our experiments respectively.

For the first sub-problem (6), we first use the singular-value decomposition $\frac{1}{q}\sum_{i=1}^{q}(I_i - C_i^{k+1}) = U \sum V^{\mathrm{T}}$ to obtain the singular value matrix $\sum$. Then the stripe component S can be solved by the following soft-thresholding operation [31]:

$$S^{k+1} = U(\mathbf{shrink}_{L_*}(\sum, \lambda))V^{\mathrm{T}} \quad (8)$$

where $\mathbf{shrink}_{L_*}(\sum, \lambda) = \mathrm{diag}\{\max(\sum_{ii} - \lambda, 0)\}_i$, $\sum_{ii}$ is the diagonal element of $\sum$.

Since L_1 norm is non-differentiable and inseparable, ADMM is used for the second sub-problem (7). Let $D_x = \nabla_x C_i$, $D_y = \nabla_y C_i$, $D_i = [D_x, D_y]^{\mathrm{T}}$, $\tau = [\tau_x, \tau_y]^{\mathrm{T}}$, sub-problem (7) equals to the following problem:

$$\begin{aligned}\{\hat{C}_i, \hat{D}_i\} = &\arg\min_{C_i,D_i} \sum_{i=1}^{q} (\frac{1}{2}\|C_i + S - I_i\|_F^2 + \tau\|D_i\|_1 \\ &+ \frac{\gamma}{2}\|D_i - \nabla C_i - \frac{\rho}{\gamma}\|_F^2), \quad i = 1, ..., q\end{aligned} \quad (9)$$

where γ is a positive parameter, ρ denotes the Lagrangian multipliers. The C-related sub-problem and D-related sub-problem are formulated as:

$$C_i^{k+1} = \arg\min_{C_i} \sum_{i=1}^{q} (\frac{1}{2}\|C_i + S - I_i\|_F^2 + \frac{\gamma}{2}\|D_i - \nabla C_i - \frac{\rho}{\gamma}\|_F^2) \quad (10)$$

$$D_i^{k+1} = \arg\min_{D_i} \sum_{i=1}^{q} (\tau\|D_i\|_1 + \frac{\gamma}{2}\|D_i - \nabla C_i - \frac{\rho}{\gamma}\|_F^2) \quad (11)$$

Fast 2D Fourier transform is used to derive C_i:

$$C_i^{k+1} = \mathcal{F}^{-1}\left(\frac{\mathcal{F}((I_i - S^{k+1}) + \nabla^{\mathrm{T}}(\gamma^k D_i^k - \rho^k))}{1 + \gamma^k(\mathcal{F}(\nabla))^2}\right) \quad (12)$$

where $\mathcal{F}$ is the Fourier operator. D_i in (11) is solved by a soft shrinkage operation:

$$D_i^{k+1} = \mathbf{shrink}_{L_1}(\nabla C_i^{k+1} + \frac{\rho_i^k}{\gamma^k}, \frac{\tau}{\gamma^k}) \quad (13)$$

where $\mathbf{shrink}_{L_1}(r, \xi) = \frac{r}{|r|} * \max(r - \xi, 0)$.

D. Cooperative Similarity Destriping (CSD)

Although the stripe noise is similar in different OCTA layers projected from the same volume image, essentially their intensities are different. The CUD model (5) will fail for this case. Therefore, we further propose a flexible cooperative similarity destriping (CSD) model to address the unequal stripe noise situation. As the stripe noise always happens in the same location, the large stripe matrix containing the stripe components of different layers should be low-rank. Here we introduce B to concatenate the stripe matrixes of different layers and $B = [S_1, ..., S_q] \in \mathbb{R}^{m \times qn}$. The CSD model is given by:

$$\min_{C_i,S_i,B} \sum_{i=1}^{q} \frac{1}{2}\|C_i + S_i - I_i\|_F^2 + \tau \sum_{i=1}^{q} \|C_i\|_{\mathrm{TV}} + \lambda \mathrm{rank}(B) \quad (14)$$

Similar to CUD, nuclear norm is used to replace the low-rank constraint:

$$\min_{C_i,S_i,B} \sum_{i=1}^{q} \frac{1}{2}\|C_i + S_i - I_i\|_F^2 + \tau \sum_{i=1}^{q} \|C_i\|_{\mathrm{TV}} + \lambda \|B\|_* \quad (15)$$

The optimization strategy of model CSD (15) is similar to model CUD (5). More specifically, ADMM is used to minimize the variables B, S_i and C_i alternatively by solving the following sub-problems:

$$\{\hat{B}, \hat{S}_i\} = \arg\min_{B,S_i} \sum_{i=1}^{q} \frac{1}{2}\|C_i + S_i - I_i\|_F^2 + \lambda \|B\|_* \quad (16)$$

$$\hat{C}_i = \arg\min_{C_i} \sum_{i=1}^{q} (\frac{1}{2}\|C_i + S_i - I_i\|_F^2 + \tau\|C_i\|_{\mathrm{TV}}) \quad (17)$$

where $I = [I_1, \cdots, I_q]$ and $C = [C_1, \cdots, C_q]$. The solution of S_i will be acquired from B:

$$S_i^{k+1} = \begin{bmatrix} B_{1,n(i-1)+1} & \cdots & B_{1,ni} \\ \vdots & \vdots & \vdots \\ B_{m,n(i-1)+1} & \cdots & B_{m,ni} \end{bmatrix} \quad (18)$$

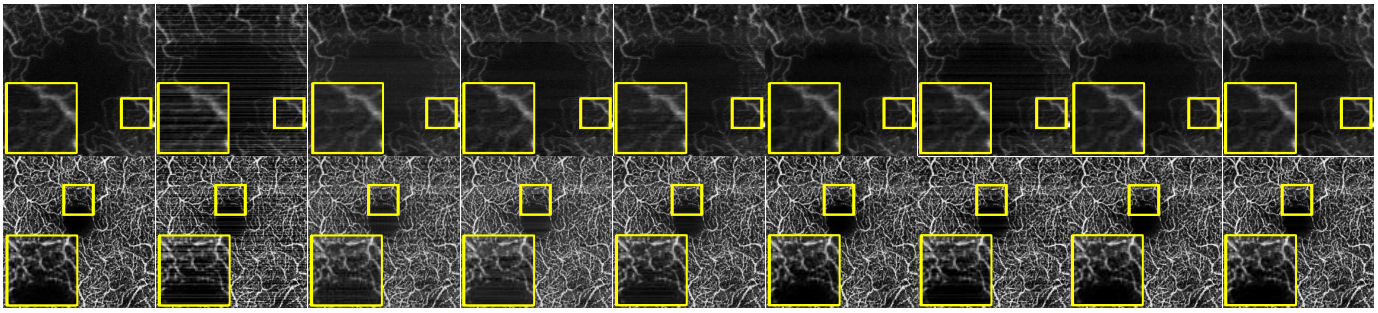

(a) Original (b) Degraded (b) FFT (c) WFT (d) VSNR (e) IDSR (f) CUD (g) CSD (h) CSD+

Fig. 4. Illustrative destriping results using different methods on two synthesized datasets. From top to bottom: FA and synthesized OCTA respectively. Representative regions (yellow border) are zoomed in for better visualization.

1) Standard optimization: The problems (16) and (17) can be solved in the similar way to CUD. Soft-thresholding operator is utilized for (16):

$$B^{k+1} = U'(\mathbf{shrink}_{L_*}(\sum{}', \lambda))V'^{\mathrm{T}} \tag{19}$$

where $(I - C^k) = U' \sum{}' V'^{\mathrm{T}}$ is the singular value decomposition of $I - C^k$.

The problem (17) is converted to a D_i-related sub-problem and a C_i-related sub-problem, which can be solved by the soft shrinkage operator (13) and the 2D Fourier transform respectively.

$$C_i^{k+1} = \mathcal{F}^{-1}\left(\frac{\mathcal{F}(I_i - S_i^{k+1}) + \nabla^{\mathrm{T}}(\gamma^k D_i^k - \rho_i^k)}{1 + \gamma^k(\mathcal{F}(\nabla))^2}\right) \tag{20}$$

2) Acceleration Solution of CSD (CSD+): Since B is q times as large as S, the standard optimization method for singular value decomposition becomes time-consuming. Here, the robust orthonormal subspace learning (ROSL) method [32] is adopted for its two advantages: same global minimum as the nuclear norm and only quadratic complexity of the matrix size. The accelerate solution of sub-problem (16) is detailed as follows.

According to [32], matrix B can be represented as $B = H\beta$, in which $H \in \mathbb{R}^{m\times p}$ is an ordinary orthonormal subspace and $\beta \in \mathbb{R}^{p\times n}$ is coefficients. B is constrained to be orthonormal, i.e. $H^T H = E_p$, where E_p is an identity matrix. In this way, the low-rank matrix B is recovered by minimizing the number of non-zero rows of β, which can be replaced by row-1 norm. Under the orthonormal subspace, S_i can be represented as $S_i = H\beta_i$, where $\beta_i = [\beta_{n(i-1)+1}; \cdots; \beta_{ni}]$. The sub-problem (16) converts to the following problem:

$$\arg\min_{\beta,H} \sum_{i=1}^{q} \frac{1}{2}\|C_i + H\beta_i - I_i\|_F^2 + \lambda\|\beta\|_{row-1} \tag{21}$$

The above problem is solved by block coordinate descent [33]. β_t and H_t can be updated efficiently as follows:

$$H_t^{k+1} = R_t^k \beta_t^{k\mathrm{T}} \tag{22}$$

$$\beta_t^k = \frac{1}{\|H_t^{k+1}\|_2^2}\mathbf{shrink}_{row-1}(H_t^{k+1\mathrm{T}} R_t^k, \frac{1}{\lambda^k}) \tag{23}$$

where $\mathbf{shrink}_{row-1}(r,\xi) = \frac{r}{\|r\|_2} * \max(\|\mathrm{r}\|_2 - \xi, 0)$ if $\|r\|_2 > 0$.

For sub-problem (17), a fast discrete homotopy method [34] is adopted in this paper. The general idea of this method is to transfer a non-linear problem to a high order linear approximation. The nonlinear PDE of (17) is :

$$\mathcal{N}(C_i(r)) = \frac{\partial C_i(r)}{\partial r} - \tau\nabla(\frac{\nabla C_i}{|\nabla C_i|_\omega}) + C_i + S_i - I_i = 0 \tag{24}$$

where r denotes the time step. $|\nabla C_i|_\omega = \sqrt{|\nabla C_i|^2 + \omega^2}$ is a smooth approximation to the non-differentiable term $|\nabla C_i|$ when ω is small and positive. Here we introduce a nonlinear operator $\mathcal{N}(\varphi(r;p))$ and rewrite (24) as follows:

$$\mathcal{N}(\varphi(r;p)) = \frac{\partial\varphi(r;p)}{\partial r} - \tau\nabla(\frac{\nabla\varphi(r;p)}{|\nabla\varphi(r;p)|_\omega}) + \varphi(r;p) + S_i - I_i = 0 \tag{25}$$

where $0 \le p \le 1$ is an embedding parameter. Expanding $\varphi(r;p)$ in the Taylor series with respect to p by supposing the series can converges at $p = 1$, we have

$$\varphi(r;p) = C_i(0) + \sum_{N=1}^{\infty} C_i(r,N),\ \ C_i(r,N) = \frac{1}{N!}\frac{\partial\varphi^N(r,p)}{\partial p^N}\bigg|_{p=0} \tag{26}$$

which must be one of the solutions of (25). To transfer the non-linear problem to a linear problem, we introduce a linear operator

$$\mathcal{L}(\varphi(r;p)) = \frac{\partial\varphi(r;p)}{\partial r} + \zeta\varphi(r;p) \tag{27}$$

with the property $\mathcal{L}(e^{-r}) = 0$ and ζ is a positive constant and set to 0.01. After using this linear operator, the solution can be obtained for $N = 1$:

$$C_i^{k+1} = C_i^{k+1}(0) + C_i^{k+1}(1) = I - S_i^{k+1} - \mathcal{H}\frac{e^{2r} - e^{-\zeta r}}{\zeta - 2}\kappa(C_i^{k+1}) \tag{28}$$

where $\kappa(C_i)$ is the approximation of curvature term $\nabla(\frac{\nabla C_i}{|\nabla C_i|_\omega})$ [34].

III. Datasets and Evaluation Metrics

The proposed methods are extensively evaluated for its effectiveness and efficiency for destriping OCTA images. In this section, a brief introduction of the used datasets is provided, followed by an introduction of all the evaluation metrics used in our experiments. All the images used in this work were collected with regulatory approvals and patients' consent as appropriate.

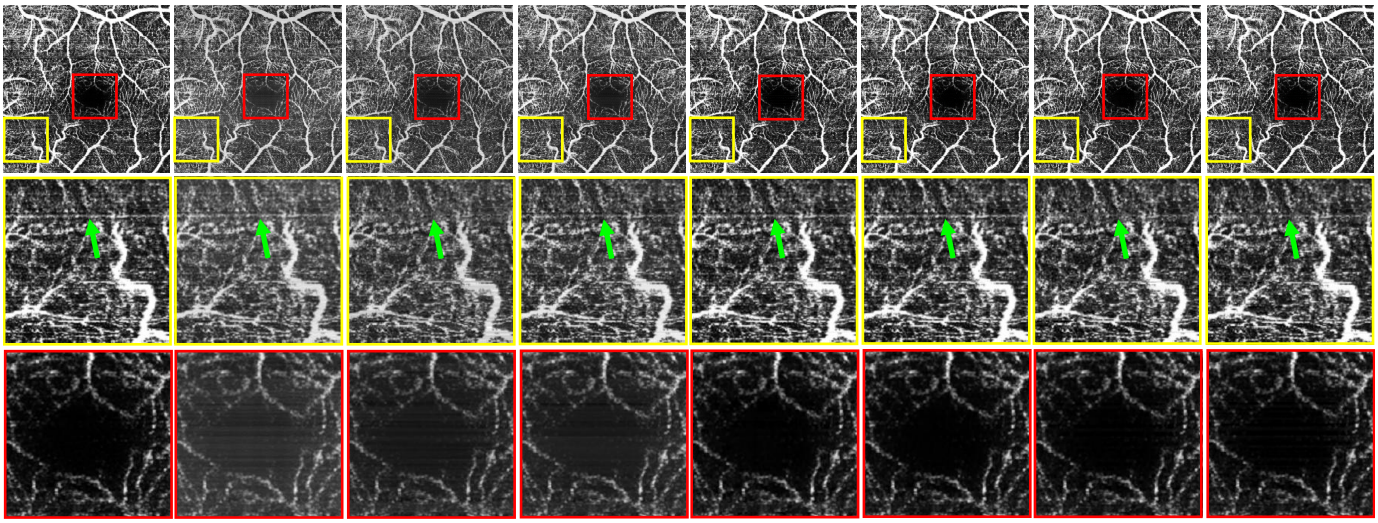

(a) Original (b) FFT (c) WFT (d) VSNR (e) IDSR (f) CUD (g) CSD (h) CSD+

Fig. 5. Example of destriping results of real OCTA images in the SVP layer by different methods. Top row: original image and its destriping results; Middle row: zoomed in view of a region (yellow border) of first row (green arrows pointing to the location of a stripe in the original and destriping results); Bottom row: zoomed-in view of the fovea (red border) of the first row.

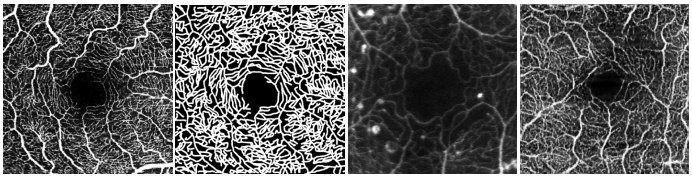

(a) Real OCTA (b) Central lines of (a) (c) FA (d) Synthetic OCTA

Fig. 6. Examples of synthetic and real datasets. Both (a) and (d) are SVP images. The central lines in (b) are thickened for better visualization.

A. Real Dataset

A real OCTA dataset consists of 340 images from 85 eyes (4 images per eye including SVP, DVP, AL and WR) that were collected from St Paul's Eye Unit, Royal Liverpool University Hospital, UK. All the images were acquired using SPECTRALIS OCT (Heidelberg Engineering, Heidelberg, Germany). The original size of each image is 840*840 pixels, covering a 3mm*3mm field of view centered at the fovea. An SVP example is shown in Fig. 6 (a). The central lines of vessels in all SVP images (see Fig. 6 (b)) were manually annotated using an in-house program by an ophthalmologist after proper training on using the program. This dataset is used to validate the effect of destriping on the vessel segmentation.

B. Synthetic datasets

All the OCTA images obtained in clinical settings are corrupted by stripe noise. There is no clean image readily for the evaluation of the performance. Following the general practice in image denoising and enhancement, we created two synthetic datasets for the purpose of comparison: one is based on fluorescein angiography (FA) whilst the other is based on synthesized clean OCTA images.

1) Synthetic images based on FA: A collection of 10 FA images from patients with diabetes by HRA2 (Heidelberg Engineering, Heidelberg, Germany) were used as the clean images. All the images have excellent quality as confirmed by visual inspection of clinicians [35]. A region of 256x256 pixels centered at the fovea was cropped and used in the experiments, as shown in Fig. 6 (c).

2) Simulated OCTA dataset: FA images are acquired by different principles from OCTA images and there is only one image per eye instead of multiple images as OCTA. To better approximate real OCTA images, we used two deep learning neural networks to generate synthesized 'clean' OCTA images from real OCTA images in two stages. In the first stage, a conditional adversarial networks [36] was used to generate vessel segmentation from the input OCTA image, which will be used by the second network. This network was trained using sixty real OCTA images and their manual annotations (The generator is trained to produce the segmentation image and the discriminator is trained to distinguish if the generated image is fake or not). In the second stage, an already trained style transfer network [37] was used to produce a synthesized 'clean' OCTA images with an OCTA image and its corresponding vessel segmentation generated in the first stage as the input. This style transfer network will preserve the content of the segmentations and the style of OCTA images. In total, synthetic 340 images of 85 eyes (four images including AL, DVP, SVP and WR per eye) were generated using the above two-stage approach. In this way, the synthesized 'clean' OCTA dataset has a similar appearance to the real dataset as shown in Fig. 6 (d).

C. Evaluation metrics

The commonly used peak signal-to-noise ratio (PSNR) and structural similarity (SSIM) [38] for measuring the quality of image denoising and enhancement [39] were to evaluate the destriping performance, whilst accuracy (Acc) and the area under the receiver operating characteristic curve (AUC) [40] were used to evaluate the segmentation results. In particular, AUC is a better metric for the overall performance measurement for imbalanced problem, i.e., in vessel segmentation problem, the vessel pixels are typically much fewer than the background pixels.

TABLE I
DESTRIPING PERFORMANCE UNDER DIFFERENT NOISE LEVELS ON TWO SYNTHESIZED DATASETS IN TERMS OF PSNR (DB)

Method	FA								Simulated OCTA							
	Small stripe intensity difference				Large stripe intensity difference				Small stripe intensity difference				Large stripe intensity difference			
	In=10 [1]	In=15	In=20	In=25	In=10	In=20	In=30	In=40	In=10	In=15	In=20	In=25	In=10	In=20	In=30	In=40
Degraded	29.36	26.01	23.74	22.05	29.36	23.74	20.72	18.73	29.08	25.83	23.56	22.03	29.08	23.63	20.61	18.76
FFT	34.71	32.47	27.97	26.18	34.71	27.97	25.86	26.20	25.58	25.33	25.49	23.38	23.38	24.21	23.69	22.94
WFT	32.01	31.47	30.72	29.87	32.01	30.72	29.06	27.25	22.68	23.44	22.76	22.03	22.68	23.23	22.17	21.38
VSNR	38.67	36.56	34.78	33.14	38.67	34.78	31.62	29.26	35.27	32.60	30.84	29.61	35.27	30.78	28.02	26.14
IDSR	33.07	32.78	31.93	31.24	33.07	31.93	30.78	28.88	29.15	29.76	28.83	27.74	29.15	28.80	27.04	26.20
CUD	33.27	34.13	32.74	29.50	33.37	33.04	29.34	24.61	34.73	30.56	27.16	24.93	33.17	27.77	23.33	20.78
CSD	34.97	34.19	33.21	32.14	35.16	33.48	31.52	29.37	36.69	**34.33**	**32.74**	**30.27**	36.51	**32.62**	**29.99**	**27.18**
CSD+	**39.30**	**37.03**	**35.17**	**33.48**	**40.25**	**35.66**	**32.32**	**29.59**	**36.71**	33.53	31.74	29.70	**37.28**	31.57	28.81	26.33

[1] In is short for intensity.

Both PSNR and SSIM are full reference metrics as they requires a noise-free image as reference.

$$PSNR = 10 \cdot \log_{10}\left(MAX_I^2/MSE\right) \tag{29}$$

where MAX_I is the maximum pixel value of the clean image and MSE is the mean squared error between the clean $C(i,j)$ and noisy image $I(i,j)$: $\frac{1}{mn}\sum_{i=0}^{m-1}\sum_{j=0}^{n-1}\|I(i,j)-C(i,j)\|^2$.

$$SSIM(x,y) = \frac{(2\mu_x\mu_y+c_1)(2\sigma_{xy}+c_2)}{(\mu_x^2+\mu_y^2+c_1)(\sigma_x^2+\sigma_y^2+c_2)} \tag{30}$$

where x and y are two images, $\mu_x, \mu_y, \sigma_x^2, \sigma_y^2$ are the mean intensity of x, y and the variance of x, y, respectively. σ_{xy} is the covariance of x and y. c_1, c_2 are two positive constants.

Acc, AUC are computed as follows:

$$Acc = (tp+tn)/(tp+fp+tn+fn) \tag{31}$$

$$AUC = (tn/(tn+fp)+tp/(tp+fn))/2 \tag{32}$$

where tp, fp, tn, fn are true positive (correctly segmented vessel pixels), false positive (incorrectly segmented vessel pixels), true negative (correctly segmented non-vessel pixels) and false negative (incorrectly segmented non-vessel pixels), respectively.

IV. EXPERIMENTAL RESULTS

In this section, the proposed CUD, CSD and CSD+ are extensively evaluated in terms of the effectiveness of destriping, efficiency of destriping and influence on vessel segmentation. We also compared the proposed models with representative destriping methods reported in the literature: fast Fourier transform (FFT) based destriping [16], wavelet-Fourier combined transform (WFT) based stripe artifact removal [15], variational model based stripe noise remover (VSNR) [23] and image decomposition based stripe removal (IDSR) [25]. The FFT and WFT are based on spectral domain. Both the VSNR and IDSR are spatial domain based optimization methods that have been applied to microscopy imaging and remote sensing imaging respectively. The source code or online executable service of these comparison methods are available on the Internet. All the experiments are carried out in MATLAB (R2018a) (Mathworks, Natick, MA) on a desktop with 8GB RAM, Intel (R) Core (TM) i5-7500 CPU @ 3.40GHz.

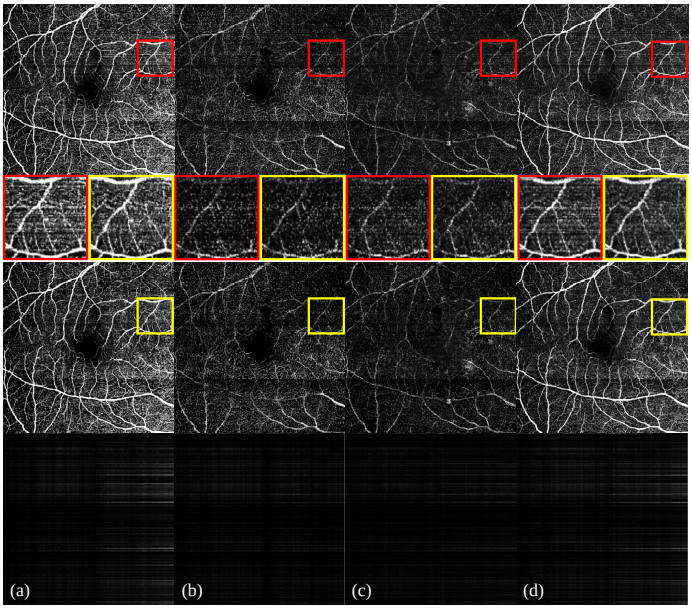

Fig. 7. Illustrative CSD+ destriping results of a real OCTA data in different layers: (a) SVP; (b) DVP; (c) AL; and (d) WR. From top to bottom: original image; a zoomed in region of the original images (red border) and destriping results (yellow border); destriping results of CSD+; estimated stripes by CSD+.

A. Effectiveness of Destriping

The effectiveness of destriping has been tested on both the real OCTA dataset and synthesized datasets. Examples randomly chosen from the synthetic and real OCTA datasets were presented for visual comparison while quantitative comparisons are presented for the synthesized datasets.

1) Experiments on Synthetic Data: To simulate stripe noise in OCTA images, we will add some synthetic stripes to the clean images in the synthetic datasets. Observed from the real stripe noise, we conclude two characteristics of the stripe noise: they are distributed randomly in an image, the stripes across different layers of a retina are located the same but have different intensities. Both of the two characteristics are considered in order to best simulate the stripe noise. Random rows of each image in the synthesized datasets are degraded by the stripe noise. For the second characteristic, we use two strategies to simulate it. The first strategy is that the

TABLE II
DESTRIPING PERFORMANCE UNDER DIFFERENT NOISE LEVELS ON THE TWO SYNTHESIZED DATASETS IN TERMS OF SSIM

Method	FA								Simulated OCTA							
	Small stripe intensity difference				Large stripe intensity difference				Small stripe intensity difference				Large stripe intensity difference			
	In=10	In=15	In=20	In=25	In=10	In=20	In=30	In=40	In=10	In=15	In=20	In=25	In=10	In=20	In=30	In=40
Degraded	0.848	0.735	0.634	0.550	0.848	0.634	0.48	0.376	0.934	0.873	0.828	0.804	0.934	0.828	0.737	0.691
FFT	0.939	0.912	0.870	0.832	0.939	0.870	0.821	0.804	0.950	0.935	0.934	0.916	0.950	0.921	0.916	0.911
WFT	0.962	0.957	0.952	0.944	0.961	0.952	0.934	0.909	0.887	0.880	0.876	0.870	0.887	0.876	0.852	0.850
VSNR	0.993	0.990	0.983	**0.974**	0.993	0.983	0.962	0.930	0.979	0.961	0.949	0.950	0.979	0.949	0.925	0.918
IDSR	0.952	0.952	0.949	0.945	0.952	0.949	0.944	0.932	0.953	0.951	0.943	0.943	0.953	0.943	0.925	0.932
CUD	0.928	0.965	0.947	0.876	0.816	0.958	0.900	0.719	0.981	0.944	0.900	0.884	0.974	0.912	0.826	0.778
CSD	0.968	0.966	0.962	0.956	0.971	0.966	0.957	0.941	**0.987**	**0.977**	**0.969**	**0.962**	0.987	**0.970**	**0.955**	**0.944**
CSD+	**0.995**	**0.993**	**0.985**	**0.974**	**0.995**	**0.984**	**0.973**	**0.954**	**0.987**	0.972	0.962	0.959	**0.988**	0.963	0.944	0.936

TABLE III
RUNTIME (IN SECONDS) FOR DESTRIPING IMAGES IN THE REAL DATASET OF DIFFERENT IMAGE SIZE

Method	Test size						Actual size
	32	64	128	256	512	1024	840
FFT	-	-	-	-	-	-	-
WFT	0.01	0.01	0.02	0.02	0.10	0.53	0.20
VSNR	0.04	0.13	0.40	2.18	24.55	135.98	50.96
IDSR	0.59	0.72	1.30	3.97	16.32	93.72	46.60
CUD	0.16	0.30	0.67	2.79	11.76	61.04	34.21
CSD	0.20	0.38	0.81	4.19	18.48	90.25	53.34
CSD+	0.03	0.08	0.26	1.31	8.73	36.48	23.93

same stripes are added to the same rows of different layers. The second strategy is that the intensity values of added stripes in different layers are different. To simulate the real OCTA dataset situation, we suppose the layer number is four (corresponding to AL, DVP, SVP, WR) in all synthesized experiments, but the models will be adapted for more images if needed. Furthermore, destriping capability of removing weak and strong stripes is tested by imitating different levels of microsaccade, i.e. the small and large intensity difference of stripes are added in the images. These two groups of intensities are set to 10, 15, 20, 25 and 10, 20, 30, 40.

For the experiments with FA images, we duplicate an FA image three times to mimic four images as of OCTA images of a retina, add the two groups stripe noise stated above. In this way, the FA simulated experiments can purely test the destriping ability without considering the different vessel structures in different layers. Tables I and II report the results in terms of PSNR and SSIM. All the methods can improve the images quality after destriping. Since the assumption of CSD is more reasonable than CUD, CSD performs better for two groups of experiments than CUD. As the added synthetic stripes conform to the preset model of VSNR, it can yield good PSNR and SSIM values in all cases. It can also be observed from these two tables that the results of CSD+ outperform the competitors for both two groups of experiments. In Fig. 4, we also provide an example for visual comparison when the added intensity of stripe noise is 40.

In view of vessel structures in different OCTA layers, the experimental results on the synthesized OCTA would be more close to those of the real OCTA images. We added the two groups of stripe noise on the synthesized AL, DVP, SVP and WR respectively. From the comparison shown in Tables I and II, CSD+ achieves 36.71 and 37.28 in PSNR, 0.987 and 0.988 in SSIM for the deepest layer AL, better than CSD. CSD performs best in other cases. CUD can achieve preferable results in the case of small noise intensity differences, while CSD shows more stable and reliable performance. An example of WR is shown in Fig. 4 for visual comparison, from which we can observe that both CSD and CSD+ can remove the added stripes whilst preserve the vessel structures.

2) Experiments on Real Data: An illustrative example of SVP image and corresponding destriping images by seven methods are shown in Fig. 5. Two regions were zoomed in to highlight the destriping cleanness and information preservation ability. The region (yellow border) with a weak stripe (green arrow) shows the destriping cleanness: FFT, VSNR, IDSR and CUD fail to remove this stripe while WFT, CSD and CSD+ succeed. The second region (red border) is from the fovea of the center of the retina and is stripe free in this example. This region is expected to remain unchanged before and after destriping. Only the low-rank based destriping method (IDSR, CUD, CSD and CSD+) can preserve the original information after destriping.

Fig. 7 shows the results of CSD+ being applied to different OCTA images from the same retina. A representative region is zoomed in to show the details of destriping results at the same location of different layers. In the zoomed-in region, stripe noise is obvious in SVP and WR but inconspicuous in AL and DVP. CSD+ considers the relationship of all the layers and removes their stripe noise in a cooperative manner. In this way, the stripes in AL and DVP can be separated with the help of SVP and WR. The estimated stripes also demonstrate that they are in the same location but having different densities.

B. Efficiency of Destriping

The efficiency of a destriping method is very important for real applications. The average running time on real OCTA images of all the methods under comparison is given in Table III. As a spectral domain based method, WFT is the fastest method. For all of the spatial domain based methods, CSD+

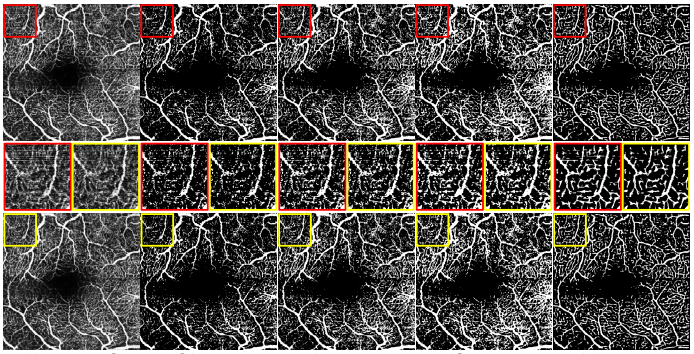

(a) Original (b) GCA (c) GMAC (d) IPAC (e) MSLD

Fig. 8. Examples of influence of destriping on vessel segmentation in real OCTA images by different segmentation methods. From left to right: original image, vessel segmentation results of GCA, GMAC, IPAC and MSLD respectively. From top to bottom: before destriping, a zoomed in region of first row (red border) and third row (yellow border), after destriping by CSD+.

is the fastest with 23.93 seconds for an 840x840 image, more than two times faster than CSD with 53.34 seconds. As CUD just needs to solve an 840x840 stripe matrix for a group of four OCTA images, it is also fast with 34.21 seconds for an 840x840 image but slower than CSD+ and poorer in destriping effectiveness.

The size of OCTA images between different vendors may be different. Thus, the efficiency of destriping methods on different image sizes is also tested. We resized the images in real OCTA dataset to $2^k * 2^k, k = 5, \cdots, 10$ and destriping them by using different methods. Table III also gives the efficiency corresponding to different image sizes. Most methods spend less than 1 second to process an image equal or smaller than 128x128. CSD+ is still the fastest spatial domain based method for large images. It just needs 36.48 seconds for a 1024x1024 image.

C. Destriping Influence on Vessel Segmentation

To investigate the destriping effect on subsequent image processing, we test its influence on vessel segmentation for the real OCTA dataset. In this way, the effectiveness of different destriping methods can also be compared indirectly. Here we adopt four segmentation methods: GCA [41], GMAC [42], IPAC [40] and MSLD [43]. The source codes of these segmentation algorithms are acquired from the authors or freely available on the Internet. All the four segmentation methods were utilized to segment the original noisy OCTA images and the destriping images produced by different destriping methods. The centerlines of the vessels from the segmentation were detected and the central lines of the segmented SVP images are compared to the centerlines from manual annotations. Quantitative results are given in Table IV in terms of Acc and AUC. After destriping, almost all the Acc and AUC values improve, which demonstrates the usefulness of destriping for vessel segmentation. CSD performs best in terms of Acc and AUC. It improves Acc from 0.7947, 0.7705, 0.7967, 0.8124 to 0.8028, 0.7783, 0.8086, 0.8162, and AUC from 0.6402, 0.6221, 0.6357, 0.6544 to 0.6479, 0.6239, 0.6461, and 0.6613 respectively. Visual comparison results are illustrated in Fig. 8. It can be observed that the segmentation performance is improved for all the segmentation methods after removing the stripe noise by CSD.

TABLE IV
QUANTITATIVE SEGMENTATION RESULTS IN TERMS OF ACC AND AUC

Method	GCA		GMAC		IPAC		MSLD	
	Acc	AUC	Acc	AUC	Acc	AUC	Acc	AUC
Original	0.7947	0.6402	0.7705	0.6221	0.7967	0.6357	0.8124	0.6544
FFT	0.7949	0.6404	0.7706	0.6223	0.7970	0.6368	0.8132	0.6546
WFT	0.7950	0.6405	0.7705	0.6222	0.7885	0.6399	0.8131	0.6552
VSNR	0.7952	0.6409	0.7708	0.6228	0.7901	0.6411	0.8133	0.6555
IDSR	0.8023	0.6385	0.7775	0.6233	0.8083	0.6452	0.8154	0.6607
CUD	0.8021	0.6471	0.7777	0.6235	0.8079	0.6453	0.8154	0.6602
CSD	**0.8028**	**0.6479**	**0.7783**	**0.6239**	**0.8086**	**0.6461**	**0.8162**	**0.6613**
CSD+	0.8027	0.6477	0.7777	0.6237	0.8081	0.6457	0.8157	0.6607

V. DISCUSSION AND CONCLUSIONS

It is important and challenging to remove stripe artifacts in OCTA images for better visualization and improved quantitative analysis of OCTA images for the management of eye disease. We have proposed two cooperative solutions (CUD and CSD) and an acceleration of CSD (CSD+) for destriping OCTA images by utilizing the intrinsic relationship of stripe noise among different en face OCTA images of the same retina. To the best of our knowledge, this is the first work to remove the stripe noise simultaneously for all the OCTA layers with convincing effectiveness and efficiency.

The proposed models utilized the low-rank constraints for stripes and also used TV regularization to preserve edges. The cooperative strategy adopted by our models not only provide better destriping performance, but also reduce the computational time to less than half compared to sequentially processing each image. In particular, with the information of the layers suffered from strong stripe noise, our models can help to separate the weak stripe noise preferably from the deep layer. CUD treats intensities of stripe noise the same for all the enface images of the same eye. It can perform well when the difference of stripe intensities is very small in different layers. On the other hand, CSD and CSD+ have better ability in dealing with the real problem as they assume stripe noise at the same locations are similar but have different intensities, which is the case in OCTA acquisition. Compared to four classic destriping methods, CSD shows its effectiveness on both two synthetic datasets especially the synthesized OCTA dataset, while CSD+ is more efficient than the other two spatial based methods (VSNR and IDSR) with higher PSNR and SSIM. To further prove the effectiveness of the destriping results, we compared the results of destriping influence on vessel segmentation. The results from four vessel segmentation methods proved that destriping is useful to improve the segmentation performance and CSD can provide the biggest improvement compared to other methods in terms of Acc and AUC. CSD+ is more than double the speed of CSD with little sacrifice of performance.

The parameters used in the proposed models are empirically chosen in our experiments. The performance could be further

improved if these parameters are fine 'tuned'. On the other hand, we have implemented the algorithms by using Matlab and by no means optimal in terms of speed. Improvement can still be made by parallel processing and GPU if needed.

Our models will be able to remove stripe noise in the vertical direction as well. In addition, OCTA images not only suffer from white bright stripe noise, but also have other kinds of noise such as short line noise and dark stripe noise. Our method has the potential to deal with both of these two kinds of noise according to Fig. 5 and Fig. 7. In the future, we will consider these two kinds of noise in our model. Our models also have potential to apply in the 3D OCTA volumes stated in [44] if q in models (5) is set to the volume size. It will be one of our works in the future. OCTA has many biomedical applications beyond eye diseases including cardiology, dermatology and oncology. Given the principle of OCTA imaging is the same, stripe noise will inevitably exist in those OCTA images. Our method is expected to be able to solve the problems in wider applications.

We are well aware of the advances of deep learning in various image processing and computer vision tasks and believe that our models can inspire new deep learning models to approach destriping problems. There is huge potential for deep learning based methods to be used to address destriping problems. The power of deep learning models relies on the training process for which the choice of loss functions can play a very important role. We conjure that the minimization problems formulated for CUD and CSD can be treated as loss functions for training deep learning models. In future work, we will explore the potential of deep learning.

In conclusion, we have proposed two cooperative destriping models and an accelerated solution to remove the stripe noise in OCTA images. The experimental results demonstrate the effectiveness and efficiency of our proposed methods in comparison to classic destriping models. Furthermore, the proposed methods prove to improve the vessel segmentation task. We expect this tool can be further optimized to become a powerful tool for clinical applications.

ACKNOWLEDGMENT

The authors thank Dr. Andong Wang from Nanjing University of Science and Technology for his valuable suggestions.

REFERENCES

[1] R. F. Spaide, J. G. Fujimoto, N. K. Waheed, S. R. Sadda, and G. Staurenghi, "Optical coherence tomography angiography," *Progress in Retinal and Eye Research*, vol. 64, pp. 1–55, 2018.

[2] H. Heimann and U. Kellner, *Atlas of fundus angiography*. Thieme, 2006.

[3] J. P. Venugopal, H. L. Rao, R. N. Weinreb, Z. S. Pradhan, S. Dasari, M. Riyazuddin, N. K. Puttiah, D. A. Rao, S. Devi, K. Mansouri *et al.*, "Repeatability of vessel density measurements of optical coherence tomography angiography in normal and glaucoma eyes," *British Journal of Ophthalmology*, vol. 102, no. 3, pp. 352–357, 2018.

[4] J. Fingler, C. Readhead, D. M. Schwartz, and S. E. Fraser, "Phase-contrast OCT imaging of transverse flows in the mouse retina and choroid," *Investigative Ophthalmology & Visual Science*, vol. 49, no. 11, pp. 5055–5059, 2008.

[5] Y. Jia, O. Tan, J. Tokayer, B. Potsaid, Y. Wang, J. J. Liu, M. F. Kraus, H. Subhash, J. G. Fujimoto, J. Hornegger *et al.*, "Split-spectrum amplitude-decorrelation angiography with optical coherence tomography," *Optics Express*, vol. 20, no. 4, pp. 4710–4725, 2012.

[6] A. C. Tan, G. S. Tan, A. K. Denniston, P. A. Keane, M. Ang, D. Milea, U. Chakravarthy, and C. M. G. Cheung, "An overview of the clinical applications of optical coherence tomography angiography," *Eye*, vol. 32, no. 2, pp. 262–286, 2018.

[7] N. Anegondi, L. Chidambara, D. Bhanushali, S. G. Gadde, N. K. Yadav, and A. Sinha Roy, "An automated framework to quantify areas of regional ischemia in retinal vascular diseases with OCT angiography," *Journal of Biophotonics*, vol. 11, no. 2, 2018.

[8] P. Zang, G. Liu, M. Zhang, C. Dongye, J. Wang, A. D. Pechauer, T. S. Hwang, D. J. Wilson, D. Huang, D. Li *et al.*, "Automated motion correction using parallel-strip registration for wide-field en face OCT angiogram," *Biomedical Optics Express*, vol. 7, no. 7, pp. 2823–2836, 2016.

[9] R. F. Spaide, J. G. Fujimoto, and N. K. Waheed, "Image artifacts in optical coherence angiography," *Retina*, vol. 35, no. 11, pp. 2163–2180, 2015.

[10] B. Braaf, K. V. Vienola, C. K. Sheehy, Q. Yang, K. A. Vermeer, P. Tiruveedhula, D. W. Arathorn, A. Roorda, and J. F. de Boer, "Real-time eye motion correction in phase-resolved OCT angiography with tracking SLO," *Biomedical Optics Express*, vol. 4, no. 1, pp. 51–65, 2013.

[11] Q. Zhang, Y. Huang, T. Zhang, S. Kubach, L. An, M. Laron, U. Sharma, and R. K. Wang, "Wide-field imaging of retinal vasculature using optical coherence tomography-based microangiography provided by motion tracking," *Journal of Biomedical Optics*, vol. 20, no. 6, pp. 1–9, 2015.

[12] M. F. Kraus, B. Potsaid, M. A. Mayer, R. Bock, B. Baumann, J. J. Liu, J. Hornegger, and J. G. Fujimoto, "Motion correction in optical coherence tomography volumes on a per A-scan basis using orthogonal scan patterns," *Biomedical Optics Express*, vol. 3, no. 6, pp. 1182–1199, 2012.

[13] J. Yang, L. Fang, Y. Hu, Y. Zhao, Y. Zheng, and J. Liu, "2D transform-domain Fourier filters for eliminating microsaccade noise in en face optical coherence tomography angiography," in *Optical Coherence Imaging Techniques and Imaging in Scattering Media III*, 2019, pp. 135–138.

[14] X. Liang, Y. Zang, D. Dong, L. Zhang, M. Fang, X. Yang, A. Arranz, J. Ripoll, H. Hui, and J. Tian, "Stripe artifact elimination based on nonsubsampled contourlet transform for light sheet fluorescence microscopy," *Journal of Biomedical Optics*, vol. 21, no. 10, p. 106005, 2016.

[15] B. Münch, P. Trtik, F. Marone, and M. Stampanoni, "Stripe and ring artifact removal with combined wavelet-fourier filtering," *Optics Express*, vol. 17, no. 10, pp. 8567–8591, 2009.

[16] W. C. Shu-wen and J.-L. Pellequer, "DeStripe: frequency-based algorithm for removing stripe noises from AFM images," *BMC Structural Biology*, vol. 11, no. 1, pp. 1–11, 2011.

[17] M. Wegener, "Destriping multiple sensor imagery by improved histogram matching," *International Journal of Remote Sensing*, vol. 11, no. 5, pp. 859–875, 1990.

[18] F. Gadallah, F. Csillag, and E. Smith, "Destriping multisensor imagery with moment matching," *International Journal of Remote Sensing*, vol. 21, no. 12, pp. 2505–2511, 2000.

[19] Y. Chang, L. Yan, H. Fang, S. Zhong, and W. Liao, "HSI-DeNet: Hyperspectral image restoration via convolutional neural network," *IEEE Transactions on Geoscience and Remote Sensing*, vol. 57, no. 2, pp. 667–682, 2018.

[20] Y. Chang, L. Yan, L. Liu, H. Fang, and S. Zhong, "Infrared aerothermal nonuniform correction via deep multiscale residual network," *IEEE Geoscience and Remote Sensing Letters*, vol. 16, no. 7, pp. 1120–1124, 2019.

[21] Y. Chang, M. Chen, L. Yan, X.-L. Zhao, Y. Li, and S. Zhong, "Toward universal stripe removal via wavelet-based deep convolutional neural network," *IEEE Transactions on Geoscience and Remote Sensing*, 2019.

[22] Y. Chang, L. Yan, M. Chen, H. Fang, and S. Zhong, "Two-stage convolutional neural network for medical noise removal via image decomposition," *IEEE Transactions on Instrumentation and Measurement*, 2019.

[23] J. Fehrenbach, P. Weiss, and C. Lorenzo, "Variational algorithms to remove stationary noise: applications to microscopy imaging," *IEEE Transactions on Image Processing*, vol. 21, no. 10, pp. 4420–4430, 2012.

[24] L. Sun, B. Jeon, Y. Zheng, and Z. Wu, "Hyperspectral image restoration using low-rank representation on spectral difference image," *IEEE Geoscience and Remote Sensing Letters*, vol. 14, no. 7, pp. 1151–1155, 2017.

[25] Y. Chang, L. Yan, T. Wu, and S. Zhong, "Remote sensing image stripe noise removal: From image decomposition perspective," *IEEE Transactions on Geoscience and Remote Sensing*, vol. 54, no. 12, pp. 7018–7031, 2016.

[26] Y. Chang, L. Yan, H. Fang, and C. Luo, "Anisotropic spectral-spatial total variation model for multispectral remote sensing image destriping," *IEEE Transactions on Image Processing*, vol. 24, no. 6, pp. 1852–1866, 2015.

[27] U. S. Kamilov, "A parallel proximal algorithm for anisotropic total variation minimization," *IEEE Transactions on Image Processing*, vol. 26, no. 2, pp. 539–548, 2016.

[28] M. Fazel, "Matrix rank minimization with applications," Ph.D. dissertation, Stanford University, 2002.

[29] E. J. Candès and B. Recht, "Exact matrix completion via convex optimization," *Foundations of Computational Mathematics*, vol. 9, no. 6, pp. 717–772, 2009.

[30] S. Boyd, N. Parikh, E. Chu, B. Peleato, J. Eckstein *et al.*, "Distributed optimization and statistical learning via the alternating direction method of multipliers," *Foundations and Trends in Machine Learning*, vol. 3, no. 1, pp. 1–122, 2011.

[31] J.-F. Cai, E. J. Candès, and Z. Shen, "A singular value thresholding algorithm for matrix completion," *SIAM Journal on Optimization*, vol. 20, no. 4, pp. 1956–1982, 2010.

[32] X. Shu, F. Porikli, and N. Ahuja, "Robust orthonormal subspace learning: Efficient recovery of corrupted low-rank matrices," in *IEEE Conference on Computer Vision and Pattern Recognition*, 2014, pp. 3874–3881.

[33] S. Bengio, F. Pereira, Y. Singer, and D. Strelow, "Group sparse coding," in *Advances in Neural Information Processing Systems*, 2009, pp. 82–89.

[34] B. Ghanbari, L. Rada, and K. Chen, "A restarted iterative homotopy analysis method for two nonlinear models from image processing," *International Journal of Computer Mathematics*, vol. 91, no. 3, pp. 661–687, 2014.

[35] Y. Zheng, J. S. Gandhi, A. N. Stangos, C. Campa, D. M. Broadbent, and S. P. Harding, "Automated segmentation of foveal avascular zone in fundus fluorescein angiography," *Investigative Ophthalmology and Visual Science*, vol. 51, no. 7, pp. 3653–3659, 2010.

[36] P. Isola, J.-Y. Zhu, T. Zhou, and A. A. Efros, "Image-to-image translation with conditional adversarial networks," in *IEEE Conference on Computer Vision and Pattern Recognition*, 2017, pp. 1125–1134.

[37] L. A. Gatys, A. S. Ecker, and M. Bethge, "Image style transfer using convolutional neural networks," in *IEEE Conference on Computer Vision and Pattern Recognition*, 2016, pp. 2414–2423.

[38] Z. Wang, A. C. Bovik, H. R. Sheikh, E. P. Simoncelli *et al.*, "Image quality assessment: from error visibility to structural similarity," *IEEE Transactions on Image Processing*, vol. 13, no. 4, pp. 600–612, 2004.

[39] Q. Yang, P. Yan, Y. Zhang, H. Yu, Y. Shi, X. Mou, M. K. Kalra, Y. Zhang, L. Sun, and G. Wang, "Low-dose ct image denoising using a generative adversarial network with wasserstein distance and perceptual loss," *IEEE Transactions on Medical Imaging*, vol. 37, no. 6, pp. 1348–1357, 2018.

[40] Y. Zhao, L. Rada, K. Chen, S. P. Harding, and Y. Zheng, "Automated vessel segmentation using infinite perimeter active contour model with hybrid region information with application to retinal images," *IEEE Transactions on Medical Imaging*, vol. 34, no. 9, pp. 1797–1807, 2015.

[41] Y. Zhao, Y. Liu, X. Wu, S. P. Harding, and Y. Zheng, "Retinal vessel segmentation: An efficient graph cut approach with retinex and local phase," *PloS One*, vol. 10, no. 4, pp. 1–22, 2015.

[42] X. Bresson, S. Esedoḡlu, P. Vandergheynst, J.-P. Thiran, and S. Osher, "Fast global minimization of the active contour/snake model," *Journal of Mathematical Imaging and Vision*, vol. 28, no. 2, pp. 151–167, 2007.

[43] U. T. Nguyen, A. Bhuiyan, L. A. Park, and K. Ramamohanarao, "An effective retinal blood vessel segmentation method using multi-scale line detection," *Pattern Recognition*, vol. 46, no. 3, pp. 703–715, 2013.

[44] M. S. S. M. M. K. J. K. G. A. H. K. J. Zhang, Y. Qiao and Y. Shi, "3D shape modeling and analysis of retinal microvasculature in OCT-Angiography images," *IEEE Transactions on Medical Imaging*, pp. 1–12, 2019.